Electrochimica Acta 443 (2023) 141983

Contents lists available at ScienceDirect

Electrochimica Acta

journal homepage: www.journals.elsevier.com/electrochimica-acta

Modelling and experimental investigation of Nb_2O_5 as a high-rate battery anode material

Jie Lin [a,b,1], Siyu Zhao [a,b,1], Thomas G. Tranter [a], Zhenyu Zhang [a,b], Fei Peng [c], Dan Brett [a,b], Rhodri Jervis [a,b,*], Paul R. Shearing [a,b,*]

[a] Department of Chemical Engineering, The Electrochemical Innovation Lab, University College London, London WC1E 6BT, United Kingdom
[b] The Faraday Institution, Harwell Campus, Didcot OX11 0RA, United Kingdom
[c] Department of Mechanical Engineering, University College London, London WC1E 6BT, United Kingdom

ARTICLE INFO

Keywords:
Niobium pentoxide
Lithium-ion battery
Characterization
Model
Charge storage

ABSTRACT

Modelling and understanding the battery electrochemical performance at high rates is a great challenge. Known for its fast rate and good cyclability, niobium pentoxide (Nb_2O_5) is a promising anode material for lithium-ion batteries and is specifically modelled and investigated in this work. Commercially sourced Nb_2O_5 was characterised using scanning electron microscopy, X-ray diffraction, and micro-computed tomography. The Nb_2O_5 material was found to contain large rod- and ball-like polycrystalline particles of tens of microns in size and have mixed T-Nb_2O_5 and H-Nb_2O_5 phases. The electrochemical performance of the material after ball milling was tested via cyclic voltammetry and constant-current cycling at different C-rates up to 50C (10,000 mA g^{-1}). The material achieved a similar charge capacity (143 mAh g^{-1}) to T-Nb_2O_5 at 0.5C and this capacity could be retained by more than 55% when C-rate was increased to 10C. The experimental results were used to support the development of the Doyle-Fuller-Newman electrochemical model for Nb_2O_5. By model parameterization, the reference exchange-current density and solid-state diffusivity of the present Nb_2O_5 were estimated to be 9.6×10^{-4} A m^{-2} and 6.2×10^{-14} m^2 s^{-1}, respectively. The model achieved accurate prediction of the battery performance up to currents of 5C with the obtained constant properties. However, the properties of Nb_2O_5 were found to be rate-dependent at higher C-rates when good agreements between the model and experiment were maintained. The decrease of the two properties at 10−50C revealed that there was a change of dominant charge storage mechanism from diffusion-controlled lithium insertion to capacitive effects, which was experimentally observed in the cyclic voltammetry.

1. Introduction

Recent progress in battery management systems (BMSs) and energy density have favored the deployment of lithium-ion batteries (LIBs) as the leading electrochemical energy storage systems [1]. However, existing battery chemistries are still far from meeting the high-power demand on electric vehicles, where charging the batteries at a comparable speed to refueling combustion engine vehicles remains a burden to the consumer, hindering its mainstream adoption. To tackle this problem, the US Department of Energy has launched a plan to develop extreme fast charging (XFC) technology that targets the addition of 200 miles of driving range in 10 min charge for electric vehicles [2].

The major obstacle to battery fast charging lies in the graphite anode which is widely employed in commercial LIBs. It has a limited solid-state diffusivity for lithium ions and is subjected to substantial degradation at high C-rates [3,4], where the C-rate refers to the inverse of time (in hours) required to fully charge/discharge the battery based on its theoretical capacity. Hence, many alternative battery anode materials are under investigation for fast charging applications [5]. Owing to its excellent rate capability at up to 60C [6], good theoretical capacity of 201.7 mAh g^{-1} [7], and robust pH and temperature stability [8], niobium pentoxide (Nb_2O_5) is an emerging and promising material for lithium-ion battery anodes and supercapacitors [9–11]. It shows great capacity and reaction rate for lithium intercalation in the potential

* Corresponding author at: Department of Chemical Engineering, The Electrochemical Innovation Lab, University College London, London WC1E 6BT, United Kingdom.
E-mail addresses: rhodri.jervis@ucl.ac.uk (R. Jervis), p.shearing@ucl.ac.uk (P.R. Shearing).
[1] These authors contributed equally to this work.

https://doi.org/10.1016/j.electacta.2023.141983
Received 10 November 2022; Received in revised form 23 January 2023; Accepted 30 January 2023
Available online 2 February 2023

window between *ca.* 1.0 and 2.0 V vs. Li^+/Li, in which formation of solid electrolyte interphase (SEI) and dendrites can be reduced [12]. Depending on the crystallization temperature and synthesis methods, Nb_2O_5 can have up to 12 different polymorphs [13], and several of them, including pseudohexagonal (TT-Nb_2O_5) [14–16], orthorhombic (T-Nb_2O_5) [8], tetragonal (M-Nb_2O_5) [17], monoclinic (B-Nb_2O_5, H-Nb_2O_5) [12,18], have been carefully explored by combining a range of modification methods such as niobium pentoxide/carbon hybrids [19, 20] and different metal species [21,22]for battery anode materials towards fast and safe energy storage.

Among these possible polymorphs, orthorhombic T-Nb_2O_5 and monoclinic H-Nb_2O_5 are widely studied due to their distinctive performance enhancement over the others. In general, the charge can be stored through different mechanisms in these materials, including diffusion-controlled lithium insertion, charge transfer with atoms on the surface or in the interlayer lattice planes (pseudocapacitance), and double-layer capacitance [23]. T-Nb_2O_5 has a special 'intercalation pseudocapacitance' behavior which allows fast two-dimensional Li+ transport within its crystal structure with no phase transition during (de)intercalation [24,25]. This mechanism endows the material with excellent rate performance and appreciable specific capacity, i.e., a supercapacitor-like feature [24]. On the other hand, H-Nb_2O_5 presents a battery-like characteristic, where lithium intercalation is controlled by diffusion and the material undergoes a phase change upon (de)lithiation [26]. As a result, H-Nb_2O_5 shows high specific capacity but moderate rate performance.

In contrast to the experimental investigations carried out on Nb_2O_5 polymorphs, very few modelling efforts have been made to understand its electrochemical performance. Battery models are important techniques to reveal the underlying physical mechanisms of the experimental phenomena and elucidate their contributions to a measurement, as well as providing the basis for advanced BMS [27,28]. To date, various battery models have been developed at multiple length and time scales, from the atomic-level density functional theory (DFT) to system-level equivalent circuit models [29,30]. The most well-known battery model is arguably the Doyle-Fuller-Newman (DFN) model developed by John Newman and colleagues [31–33], which is often applied to simulate cell performance [34] and can account for electrode microstructure [35]. However, the feasibility of the battery models at high C-rate cycling is unclear and has not been widely discussed. The complex physics and microstructure in the battery which are normally simplified or neglected in many cell-level models, can have significant impacts on the cell behaviours at high C-rates. Therefore, modelling high-rate battery performance is very challenging and crucial in many high-power applications. It is desirable to develop an electrochemical model at high C-rates, using Nb_2O_5 as an exemplar, and simulate its performance at a wide range of C-rates. Through parameterization of its key physicochemical properties, we believe that the battery electrochemical model can give us insights into the key charge storage mechanisms of Nb_2O_5.

Herein we establish a DFN electrochemical model to investigate the performance of Nb_2O_5 for the first time and parameterise its important physicochemical properties with the support of multiscale characterization. A commercial Nb_2O_5 material obtained from mass production without careful nanostructuring and crystal phase control was adopted for electrochemical energy storage. The X-ray diffraction (XRD) analysis indicates that the material is a mixture of T-Nb_2O_5 and H-Nb_2O_5 phases. The battery material is tested at C-rates up to 50C. It exhibits a battery-like behavior at low C-rates as the charge capacity is dominated by diffusion-controlled lithium insertion, whereas the pseudocapacitance dominates the charge storage behavior at high C-rates. Through parameterising and tracking the significant changes of exchange current density and solid-state diffusivity, we demonstrate that the battery model can be an effective tool to predict the electrochemical performance of Nb_2O_5 and capture the evolution of its charge storage mechanism.

2. Experimental

2.1. Sample fabrication

Commercial niobium (V) oxide (Nb_2O_5) was purchased from Sigma-Aldrich (UK) Co., Ltd. The received Nb_2O_5 is a mixture of large clusters and powders. In this case, the Nb_2O_5 was ball milled at 350 rpm for 3 h to reduce its particle size which is suitable for further battery ink preparation and lithium intercalation. To prepare the Nb_2O_5 working electrodes, 80 wt% ball-milled Nb_2O_5, 10 wt% conductive carbon black (Timical Super P C65, Imerys) and 10 wt% polyvinylidene difluoride (PVDF, Solvay) were dissolved in N-methyl-2-pyrrolidone (NMP, Fisher Scientific) solution and mixed in a planetary centrifugal mixer (Thinky ARE-250) to form a viscous slurry. The slurry was cast onto a 20 μm thick aluminium foil using a doctor blade (Elcometer 3580) and dried on a heating plate at 60 °C for 3 h and subsequently in a vacuum oven at 80 °C overnight. The electrode coating was then calendered to a uniform thickness and punched into circular electrodes with 15 mm diameter. The mass of the electrodes was weighed accurately by an analytical balance (Ohaus; $\delta = 0.01$ mg), and the areal mass loadings of Nb_2O_5 were measured to be 2.0−2.5 mg cm^{-2}.

Standard CR2032 coin cells (Hohsen) were assembled in an argon-filled glovebox (O_2<0.5 ppm, H_2O<1.0 ppm), with lithium metal foil (15.6 mm diameter, 250 μm thick, PI-KEM) as the counter electrode, glass microfiber separator (GF/A, Whatman), and 100 μL 1.0 M $LiPF_6$ in (1:1 vol%) ethylene carbonate/dimethyl carbonate (EC:DMC, Solvionic) electrolyte.

2.2. SEM and XRD analysis

The morphology and microstructures of samples were characterized by scanning electron microscope (SEM) (ZEISS Evo MA10 and ZEISS GeminiSEM 360). X-ray diffraction (XRD) patterns were obtained by Rigaku Smartlab XRD with a Cu X-ray radiation source. Rietveld refinement was performed in GSAS-II software. For the commercial Nb_2O_5 material, the unit cell parameters and background were refined and used as the initial structure. The unit cell parameters and phase ratios are allowed to vary. The pattern was fit between 20^o and 50^o 2θ values.

2.3. Micro-CT characterization

A 1 mm disc of as-prepared electrode was cut by laser (A Series/ Compact Laser Micromachining System, Oxford Lasers), and was mounted on the head of a pin by epoxy resin. The prepared sample was then scanned by lab-based X-ray micro- Computed Tomography (CT) system (Zeiss Xradia 620 Versa, Carl Zeiss). A total of 1201 projections were acquired over a 360^o rotation with an exposure time of 10 s per projection. The sample was placed between the X-ray source and detector providing a voxel resolution of 396 nm using the 20 × objective magnification. The micro-CT was operated at 140 kV source acceleration voltage.

Micro-CT projections were reconstructed using a filtered-back projection algorithm (XMReconstructor, Carl Zeiss Inc.). The reconstructed micro-CT datasets were imported into Avizo 2022.1 (ThermoFisher) for further segmentation and quantification. A median filter was applied to increase the signal to noise ratio. The scans of the pristine material, imaged by micro-CT, were segmented (based on grayscale values) into two phases consisting of active materials and the background (carbon binder domain, CBD, and pore space).

2.4. Electrochemical testing

The electrochemical tests of the coin cells were performed in a BCS-805 BioLogic battery cycler. The cells were cycled between 1.2 and 3.0 V vs. Li^+/Li. The pseudo-open-circuit potential (OCP) of Nb_2O_5 was

measured at a charge/discharge rate of C/25, where the C-rate is calculated based on the theoretical capacity of Nb_2O_5 at 201.7 mAh g^{-1}. Cyclic voltammetry (CV) tests were carried out at scan rates of 0.1, 0.2, 0.5, 1, 2, 5 mV s^{-1}. Rate capability tests were conducted in a wide range of C-rates from 0.5C to 50C, and each galvanostatic discharge/charge was carried out after a constant current-constant voltage (CC-CV) charge/discharge until the current decayed to C/100.

3. Modeling

In this work, a full Doyle-Fuller-Newman (DFN) battery electrochemical model is employed to simulate cell performance and parameterize the key physicochemical properties of Nb_2O_5. This model is developed from the porous electrode and concentrated solution theories in a pseudo-2D geometry, which assumes homogenously distributed spherical electrode particles within the Nb_2O_5 porous electrode. As shown in Fig. 1, the entire cell is simplified into 1D layers of aluminium current collector, Nb_2O_5 working electrode, lithium counter electrode and separator, and another 1D along the radial direction of electrode particles is considered for lithium intercalation into Nb_2O_5.

Charge balances in both the solid and liquid phases of Nb_2O_5 working electrode are considered as below:

$$\nabla\cdot\vec{i}_s = -ai \tag{1}$$

$$\nabla\cdot\vec{i}_l = ai \tag{2}$$

where $\vec{i}_s = -\sigma\nabla\phi_s$, $\vec{i}_l = -\kappa\nabla\phi_l + \frac{\kappa_D RT}{F}\nabla\ln c_l$. $\vec{i}_s$ and $\vec{i}_l$ are the solid-phase and liquid-phase current density; a is the specific interfacial surface area within the porous electrode; i is the reaction current per unit area of the pore surface; ϕ_s and ϕ_l are the solid-phase and liquid-phase electrical potentials, respectively; σ and κ are the effective electrical conductivity in the solid and liquid, respectively; κ_D is the effective conductivity associated with concentration overpotential; R is the universal gas constant and F is Faraday's constant; T is temperature.

The liquid-phase mass balance of Nb_2O_5 working electrode is expressed as:

$$\varepsilon\frac{\partial c_l}{\partial t} + \nabla\cdot\vec{N}_l = \frac{ai}{F} \tag{3}$$

where $\vec{N}_l = -D_l\nabla c_l + \frac{\vec{i}_l t_+^0}{F}$. t is time, ε is the electrode porosity, c_l is the liquid-phase salt molarity, and $\vec{N}_l$ is the superficial salt flux; D_l is the liquid-phase Fickian salt diffusivity, and t_+^0 is the cation transference number.

The intercalation dynamics in solid electrode particles is governed by Fickian diffusion as:

$$\frac{\partial c_s}{\partial t} = \frac{D_s}{r^2}\frac{\partial}{\partial r}\left(r^2\frac{\partial c_s}{\partial r}\right) \tag{4}$$

Here, r is radial position within the intercalation particle at a given location, c_s is the molar concentration, and D_s is the solid-phase diffusivity of lithium in the intercalation particle. A zero-flux condition is defined at the center of the active particles and a Neumann boundary condition is used to relate the interfacial current density i to the concentration gradient, expressed as:

$$-D_s\frac{\partial c_s}{\partial r}\Big|_{t,0} = 0,\ -D_s\frac{\partial c_s}{\partial r}\Big|_{t,r_0} = \frac{i}{F} \tag{5}$$

where r_0 is the average radius of the solid electrode particles.

The charge transfer on the electrode-electrolyte interface is calculated via Butler-Volmer kinetics:

$$i = i_0\left[\exp\left(\frac{\alpha F\eta}{RT}\right) - \exp\left(-\frac{(1-\alpha)F\eta}{RT}\right)\right] \tag{6}$$

where $i_0 = i_{0,\mathrm{ref}}(c_{s,\max} - c_{s,\mathrm{surf}})^{\alpha}c_{s,\mathrm{surf}}^{1-\alpha}c_l^{\alpha}$, $\eta = \phi_s - \phi_l - E_{\mathrm{eq}}$. i_0 is the exchange-current density, α is the symmetry factor, η is the surface overpotential; $i_{0,\mathrm{ref}}$ is the reference exchange-current density, $c_{s,\max}$ is the maximum lithium concentration that is allowed in the solid electrode, and $c_{s,\mathrm{surf}}$ is the surface concentration of electrode particles; E_{eq} is the equilibrium potential of the material.

For the lithium counter electrode, the lithium ions are assumed to be stripped or plated on the electrode surface and the intercalation dynamics are ignored. Eq. (6) is used to calculate the charge transfer of lithium stripping/plating with the exchange-current density defined as [36]:

$$i_0 = i_{0,\mathrm{ref}}c_{\mathrm{Li}}^{1-\alpha}c_l^{\alpha} \tag{7}$$

where c_{Li} is the lithium concentration of lithium metal.

The above DFN model has been established on an open-source Python Battery Mathematical Modelling (PyBaMM) platform [37,38]. The platform employs state-of-the-art automatic differentiation and numerical solvers and can compute the model differential equations as fast as within 0.1 s. Hence, we adopt the DFN model in PyBaMM to simulate the electrochemical tests of Nb_2O_5 vs Li^+/Li in half cells.

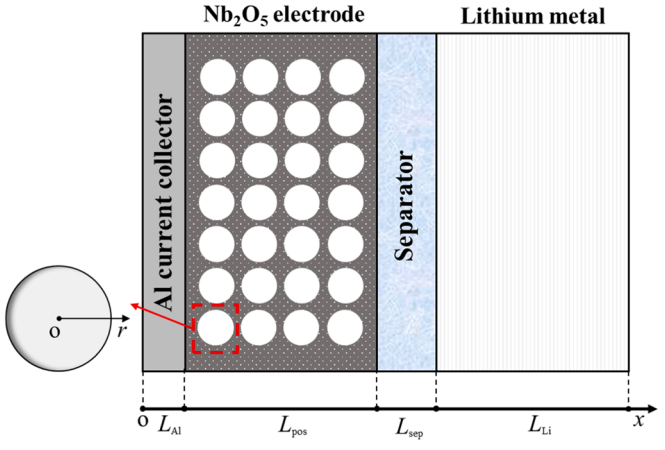

Fig. 1. P2D model geometry of Nb_2O_5 half-cells.

4. Results and discussions

4.1. Structural characterization

The morphologies of the material were firstly studied by SEM. The size of commercial Nb_2O_5 secondary particles was found to be around tens of microns and showed a mixture of rod and ball structures as illustrated in Fig. 2a. Although one of the advantages of Nb_2O_5 electrodes is their ability to have fast diffusion even with large size distributions, the original large-size particles would likely exhibit a significant diffusion resistance at high C-rates and were therefore considered unfavorable for making battery electrodes. The raw Nb_2O_5 powder was thus processed by ball mill and prepared as the working electrode. The high-magnification SEM image (Figs. 2b and S1) demonstrated that the majority of the ball milled Nb_2O_5 particles were reduced to around 1 micron in size, which is beneficial for electrolyte diffusion and lithium intercalation. This unique structure provides more surface area between the electrode and electrolyte and facilitates rapid charge and discharge.

An XRD pattern of the commercial Nb_2O_5 is shown in Fig. 2c. The XRD peaks of the material at 22.6°, 28.4°, 28.9° and 36.6° can be indexed to (001), (180), (200) and (181) planes of T-Nb_2O_5 (PDF No. 30-0873) [15]. The XRD peaks at 23.7°, 38.9° and 47.5° could be assigned to (110), (-713) and (704) planes of H-Nb_2O_5 (PDF No. 37-1468) [15].

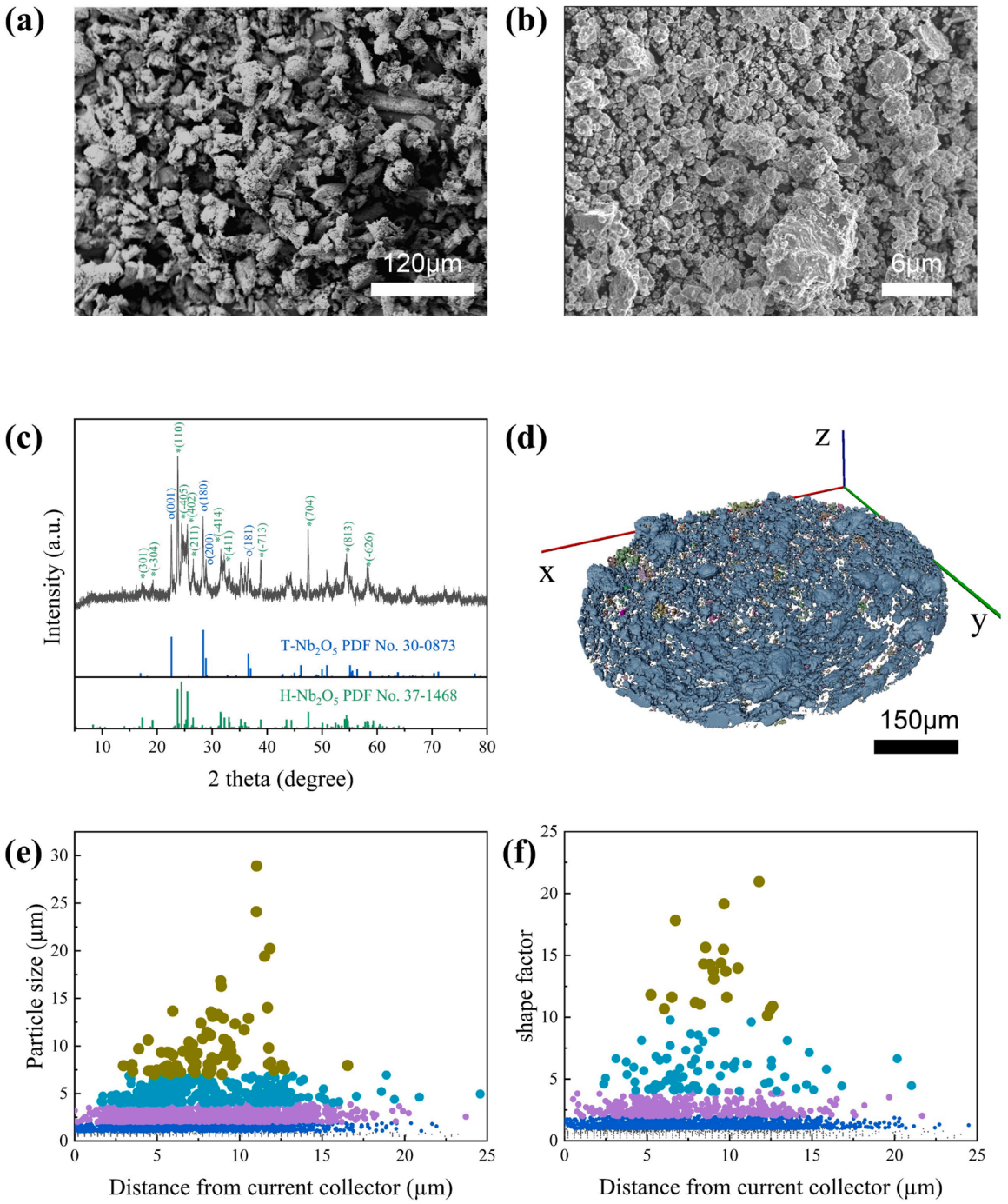

Fig. 2. SEM images of commercial Nb_2O_5 (a) before (low magnification) and (b) after (high magnification) ball milling. (c) XRD pattern of commercial Nb_2O_5. (d) Reconstructed CT image of particles of commercial Nb_2O_5 electrode. Spatial distribution of (e) particle sizes and (f) shape factor of commercial Nb_2O_5 electrode.

The XRD results indicated the main structure of commercial Nb_2O_5 was a mixture of T-Nb_2O_5 (32.2 wt%) and H-Nb_2O_5(67.8% wt%) according to XRD refinement and fitting result (Fig. S2).

The macroscopic 3D morphology of the fabricated commercial Nb_2O_5 electrode was examined using X-ray micro-CT, which depicted the Nb_2O_5 particles distribution in 3D space (Fig. 2d–f). After extracting the active material phase according to the grey scale level using thresholding segmentation, the distribution of the active materials can be visualized (Fig. 2d). Fig. 2e shows the spatial distribution of particle sizes, which demonstrates the sizes of particles varying from 0.5 to 29 μm and the particles show a homogeneous spatial distribution. Hence the particle size distribution of the entire electrode can be analyzed in Fig. S3 and fitted by a lognormal function. The mean particle diameter based on the number of particles for each size is calculated to be 1 μm, which will be used for model simulation. In addition, the shape factor f of the particles, which describes their sphericity, is defined as:

$$f = \frac{A^3}{36\pi V^2} \tag{8}$$

where A and V are the area and volume of particles in 3D space.

As the shape factor approaches 1, the particle is closer to a perfect sphere. Fig. 2f illustrates the spatial distribution of shape factor for the prepared electrode. It is observed that the majority of particles possess a shape factor below 6 and the particles are evenly distributed across the

electrode thickness.

4.2. Electrochemical tests

The electrochemical tests were performed on the Nb_2O_5 half cells, as outlined in Section 2.4. The first three cycles of the pseudo-OCP measurements are presented in Fig. 3a. The initial discharge (lithiation) capacity at 196.7 mAh g^{-1} was close to the Nb_2O_5 theoretical capacity (201.7 mAh g^{-1}). However, the first charge (delithiation) capacity was only 150.4 mAh g^{-1}, followed by similar capacities in later cycles. This reveals an irreversible capacity loss in the initial cycle of Nb_2O_5 [12,26]. The effect of the ball milling process was instigated by comparing it to a raw Nb_2O_5 sample which was assembled into half cells and its pseudo-OCP measurements are provided in Fig. S4. It was observed that the the ball milling process could help to improve cell capacity and rate capability, although there was a drop of initial Coulombic efficiency from 89 to 76% possibly due to more defects in the crystal structure and increased surface areas for irreversible structural change and parasitic electrochemical reactions [39]. Furthermore, the pseudo-OCP of the present Nb_2O_5 (a mixture of T- and H-Nb_2O_5) is normalized in SOC% and compared with those of single T-Nb_2O_5 and H-Nb_2O_5 [12] in Fig. 3b. As can be seen, T-Nb_2O_5 has a nearly linear decrease in OCP between 10 and 100% SOC, whereas the OCP of H-Nb_2O_5 has a voltage plateau at 1.6−1.7 V due to the phase transition during (de)lithiation. As a result, the present Nb_2O_5 exhibits a very similar OCP curve to T-Nb_2O_5, but still has a small and visible plateau at 1.65 V (see Fig. 3a), indicating the influence of the H-phase identified via XRD.

Cyclic voltammetry (CV) tests were further conducted on the present Nb_2O_5. Fig. 3c shows the CV measurements at 0.1 mV s^{-1} for the first three cycles between 1.2 and 3.0 V (vs. Li^+/Li). The CV curves in the second and third cycle slightly deviated from the first formation cycle but remained stable. The material exhibits a wide window of redox reactions in the voltage range of 1.2–2.2 V, and a pair of cathodic and anodic peaks were clearly observed at 1.60 and 1.75 V, respectively, which correspond to the reactions of the Nb^{5+}/Nb^{4+} couples. This indicates that the present Nb_2O_5 has a battery-like behavior where the lithiation is dominated by diffusion-controlled lithium insertion in the solid state. CV curves at various scan rates of 0.1–5.0 mV s^{-1} are presented in Fig. 3d. As the scan rate increased, the cathodic peak (I) became less obvious and shifted to below 1.2 V (out of the test range) at 5.0 mV s^{-1}, while the anodic peak (II) shifted to higher voltages due to polarization and expanded to a wider voltage window.

Furthermore, the reaction current (I) at a characteristic site of the CV diagram can be correlated with the scan rate (v) using the following power function [6,8,40]:

$$I(v) = av^b \tag{9}$$

where a and b are coefficients to be fitted. The value of b can vary from 0.5 to 1.0 and give insights into the dominant charge storage mechanisms of the material. b=0.5 represents a diffusion-controlled insertion process which is the case for most battery materials; b=1.0 indicates a capacitive charge storage like most supercapacitors.

Accordingly, the source of reaction current at a certain voltage can be broken down into the lithium insertion (k_1v) and capacitive effects ($k_2v^{1/2}$) [23], expressed as:

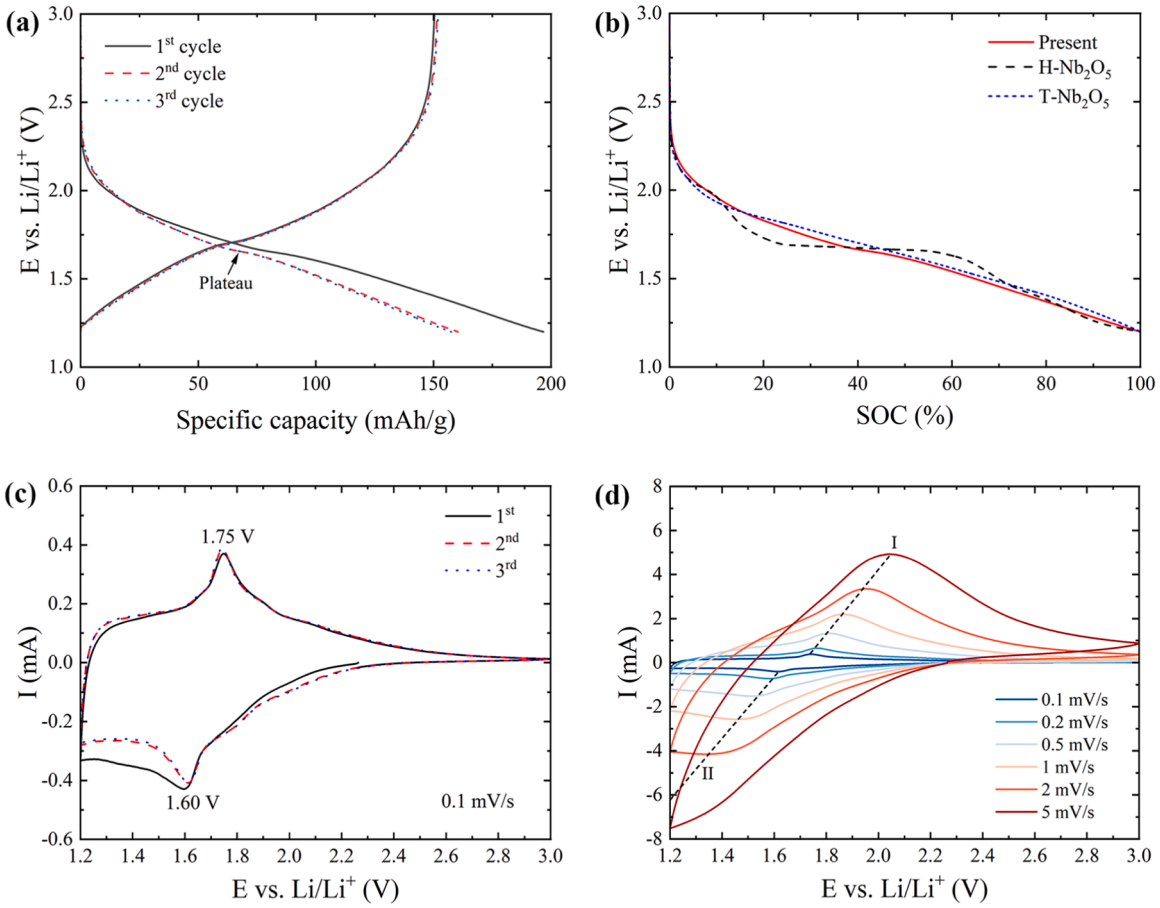

Fig. 3. (a) Pseudo-OCP of Nb_2O_5 for the first three cycles tested at C/25 between 1.2 and 3.0 V vs. Li^+/Li. (b) Pseudo-OCP of present Nb_2O_5 in comparison with H-Nb_2O_5 and T-Nb_2O_5. The capacities were rescaled to 0−100%SOC. The data for H- and T- were obtained from [12]. Cyclic voltammetry of Nb_2O_5 (c) for the first three cycles at 0.1 mV s^{-1} scan rate and (d) at 0.1−5 mV s^{-1} scan rates.

$$I(v) = k_1 v^{1/2} + k_2 v \quad (10)$$

where k_1 and k_2 are fitted parameters.

Eq. (9) was used to fit the reaction current of the cathodic (I) and anodic (II) peaks at different scan rates and obtain their b values in Fig. 4a. The b values of peak I (b_I) and peak II (b_{II}) are 0.67 and 0.78, respectively, both of which are close to 0.5 and reveal a diffusion-controlled lithium insertion dominating the charge storage. Moreover, the reaction current over the entire CV (*cf.* Fig. 3d) was fitted by Eq. (10), and the contribution of the capacitive effect to the electrochemical reaction was quantified. An example of 5 mV s^{-1} scan rate (equivalent to 10C) is given in Fig. 4b, where the capacitive effect is highlighted by the shaded area on the CV curve. The percentage of overall capacitive effect over the full voltage window is estimated by its enclosed area at 53.4%, and charge storage at voltage above 2.0 V is found to be dominated by capacitance as the material's state of lithiation is approaching 0. The contributions of capacitance at different scan rates are summarized in Fig. 4c. It is clear that the capacitive effect contributes only a small percentage to the charge transfer at lower scan rates. The majority of lithium ions are still stored through diffusion-controlled insertion in the present Nb_2O_5. It is also expected that the capacitive effect is more pronounced at higher scan rates, as the rate of charge transfer and lithium intercalation is limited to fulfil the required scan rate and the rest will be supplemented by capacitance.

Rate capability tests were performed on the Nb_2O_5 cells for C-rates up to 50C, and each C-rate was repeated for 3 cycles. As Nb_2O_5 is an anode material, its charge (delithiation) capacity from 1.2 to 3.0 V vs. Li^+/Li, which corresponds to discharge in a full-cell configuration, is reported in Fig. 5a. The variation of cell specific capacity for every 3 cycles at the same rate was less than 3.0%, hence cell voltage responses of the second cycle at each C-rate are provided in Fig. 5b. The average charge capacity for the present material at 0.5C was 143 mAh g^{-1}, and more than 55% of the capacity (referring to 0.5C) was retained when the applied current is below 10C. There was still 29 mAh g^{-1} charge capacity remaining at 50C. This result demonstrates a good rate capability of the material which can satisfy most fast discharging/charging applications [2,37]. At 20 and 50C, cell capacity was limited by large polarization and mainly contributed by capacitance, so the capacity retention was reduced to 41% and 20%, respectively, while still exhibiting a reasonable amount of charge storage. The electrochemical performance of the present Nb_2O_5 is compared with similar Nb_2O_5 anodes from the literature in Table 1. To enable a fair comparison, only data for Nb_2O_5 cycled in the same voltage range (1.2−3.0 V vs. Li^+/Li) as the present study were collected, and their specific capacities tested at 0.5C (if available) were compared. The maximum rate capability tested in different studies were also reported. It could be observed that the Nb_2O_5 material tested in this study showed comparable capacity at 0.5C with T-Nb_2O_5, TT-Nb_2O_5 and amorphous Nb_2O_5 [12,41], but slightly worse than specially nanostructured H-Nb_2O_5 [12,42] and T-Nb_2O_5 [43], all of which were developed for battery energy storage. The rate performance of the present Nb_2O_5 was superior or similar to most of the developed Nb_2O_5 at identical C-rates (e.g., 5C, 50C), with the only exception being H-Nb_2O_5 nanowire [42].

In addition, the charge-discharge cycle performance of the present Nb_2O_5 was tested at 5 and 10C and are provided in Fig. 5c-d. The initial specific capacity of the material was 105 mAh g^{-1} and 76 mAh g^{-1} at 5C and 10C, respectively, and it could still retain *ca.* 98 mAh g^{-1} (94%) and 70 mAh g^{-1} (92%) capacity after 200 cycles. Hence, the present Nb_2O_5 was deemed promising for high-power battery energy storage, and a suitable example for development and investigation of the DFN model in high C-rate applications, as well as physicochemical parameterisation of Nb_2O_5.

4.3. Model parameterization

Battery modelling can give insights into the material properties, fundamental electrochemical processes, and cell performance. Here we applied the DFN electrochemical model to simulate the cell rate performance tests (*cf.* Fig. 5) and parameterise key physicochemical properties, i.e., reference exchange-current density ($i_{0,ref}$) and solid-state diffusivity (D_s), of the present Nb_2O_5. The cell voltage at 0.5C was used to train the battery model, where a cost function (g) is defined as the error between the simulated (V_t^{sim}) and experimental (V_t^{exp}) voltage and minimized by fitting the properties via a nonlinear least squares approach [44], expressed as below:

$$g = \sum_{t=1}^{N} \left(\frac{V_t^{sim} - V_t^{exp}}{\Delta V^{exp}} \right)^2 \quad (11)$$

where ΔV^{exp} is the cell voltage range.

A detailed list of model parameters to set up the battery model are provided in Table 2. The OCP of Nb_2O_5 was taken from Fig. 3, and the electrolyte properties (e.g., effective ionic conductivity, diffusivity) were provided by Landesfeind et al. [45] which have been well documented in the PyBaMM library.

The model parameters obtained at 0.5C were employed to simulate cell performance at other C-rates and validated against the test results. The comparison between experiments and simulations at 0.5−5C are plotted in Fig. 6a. At 0.5C, the reference exchange-current density ($i_{0,ref}$) and solid-state diffusivity (D_s) of Nb_2O_5 were parameterized to be 9.6 × 10^{-4} A m^{-2} and 6.2 × 10^{-14} m^2 s^{-1}, respectively. This allowed the simulated voltage to agree with the experiment within 40 mV maximum discrepancy. The parameters were demonstrated to be reliable when being verified with tests at 1, 2 and 5C, where the predicted cell voltage deviated from the experiment by 300 mV at most which appears at the beginning of charge. However, when the applied current was extended to 10C and above, significant differences were observed between the simulations and experiments (see short dash lines in Fig. 6b). This occurrence is attributed to the changes in the cell electrochemical processes and the limitations of the DFN model applied here. As has been

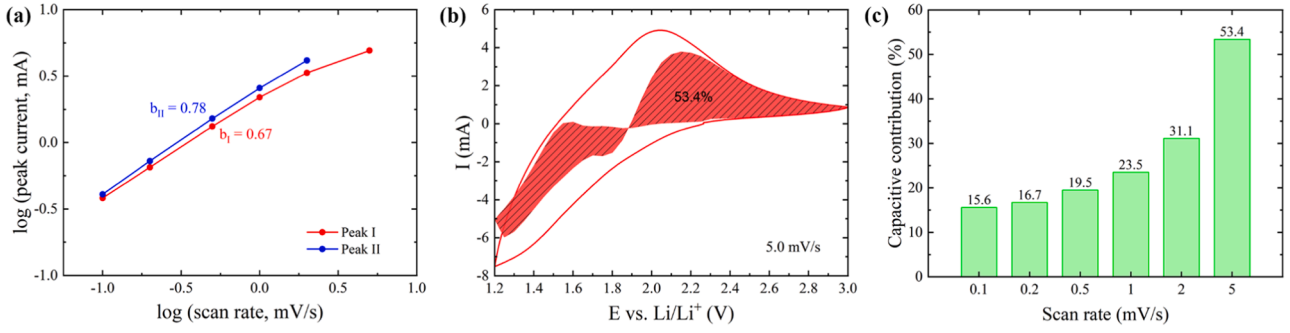

Fig. 4. (a) Fitting of b values for anodic peak I (b_I) and cathodic peak II (b_{II}) with Eq. (9). (b) Capacitive contribution (red shadow area) to the overall electrochemical reactions at 5 mV s^{-1} scan rate. (c) Capacitive contributions at 0.1−5 mV s^{-1} scan rates.

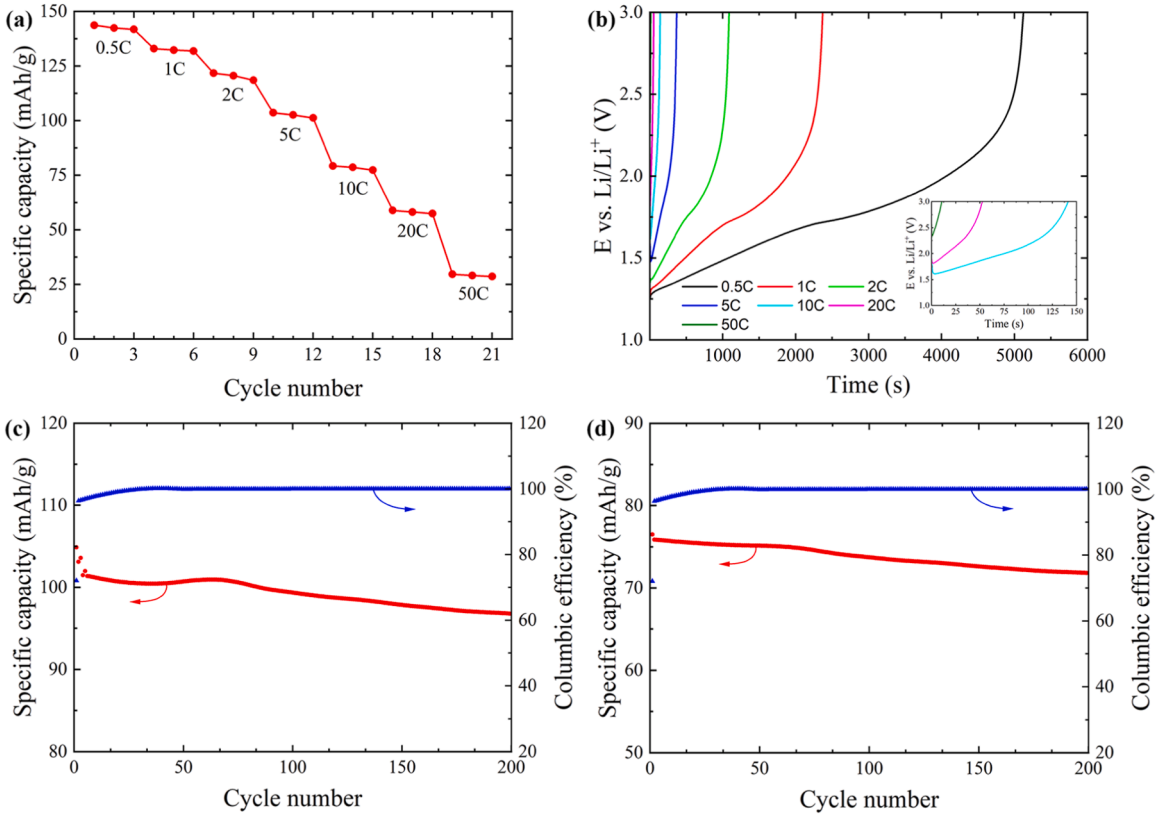

Fig. 5. (a) Specific capacity and (b) Cell voltage of Nb_2O_5 at different C-rates between 0.5 and 50C. Data for 10−50C are highlighted on the inset. Each C-rate was tested for three cycles, and the cell voltage at the second cycle was plotted. Galvanostatic charge-discharge cycle performance at (c) 5C and (d) 10C.

Table 1
Summary of the electrochemical performance of Nb_2O_5 anodes.

Material	Capacity mAh g^{-1}	Rate capability mAh g^{-1}	Voltage range V vs. Li^+/Li	Refs.
T-Nb_2O_5	156@0.2C	8@60C	1.2−3.0	[12]
T-Nb_2O_5	127@0.5C	114@5C	1.2−3.0	[41]
T-Nb_2O_5 nanobelt	205@0.5C	54@50C	1.2−3.0	[43]
H-Nb_2O_5	181@0.2C	25@5C	1.2−3.0	[12]
H-Nb_2O_5 nanowire	176@0.5C	139@2.5C	1.2−3.0	[42]
TT-Nb_2O_5	164@0.5C	80@5C	1.2−3.0	[41]
amorphous Nb_2O_5	93@0.5C	47@5C	1.2−3.0	[41]
Present work	143@0.5C	102@5C, 29@50C	1.2−3.0	

Table 2
Model parameters of Nb_2O_5 used in the DFN model.

Parameter	Symbol	Nb_2O_5	Separator	Li metal
Thickness (μm)	L	48	30	250
Particle radius (μm)	r_0	1.0	–	–
Effective electrical conductivity (S m^{-1})	σ_s	100	–	1.1×10^7
Maximum Li concentration (mol m^{-3})	$c_{s,max}$	33,633	–	76,900[36]
Initial electrolyte concentration (mol m^{-3})	c_{l0}	1000		
Porosity (−)	ε	0.90	0.66	–
Symmetry factor (−)	α	0.5	–	0.3[36]
Reference exchange-current density (A m^{-2})	$i_{0,ref}$	9.6×10^{-4} f	–	3.38×10^{-3} [36]
Solid-state diffusivity (m^2 s^{-1})	D_s	6.2×10^{-14} f	–	–

Note: "f" stands for "fitted".

seen in the CV diagram (*cf.* Fig. 4), charge storage at C-rates beyond 10C starts to be dominated by capacitance, whereas this physics has not been thoroughly considered in the DFN model and its contribution is often lumped in the effective charge transfer and lithium diffusion rates. This requires the model parameters to be adjusted or refitted to take into account the change of charge storage mechanism. The refitted cell voltages are presented in Fig. 6b at 10C−50C, and the values of $i_{0,ref}$ and D_s over the entire C-rate range are shown in Fig. 6c and d. By tuning the relevant parameters, the DFN model is still able to fit the experiment at extremely high C-rates. The drops of fitted $i_{0,ref}$ and D_s at high C-rates, particularly $i_{0,ref}$ which decreases by 3 orders of magnitude at 50C, indicate reduced charge transfer rate and lower contribution from diffusion-controlled lithium insertion. Instead, the large polarisation at high C-rates drives more lithium ions to be stored in near-surface or interlayer lattice planes. In consistence with $i_{0,ref}$, D_s is reduced by one order of magnitude to 8.0×10^{-14} m^2 s^{-1} at 50C. The variation is slightly minor to $i_{0,ref}$, as lithium insertion into the Nb_2O_5 crystal interlayer space is fast and not largely affected by C-rates which has been shown in T-Nb_2O_5 [8]. The magnitude of D_s characterised via the DFN model agreed well with that from a GITT approach where it was found in the range of 10^{-14}–10^{-15} m^2 s^{-1} for T-Nb_2O_5 and H-Nb_2O_5 [26].

Besides, the heterogeneity of electrode microstructure can play an important role at high C-rates, which may affect the concentration gradient and electrode wetting and consequent effective values of material properties. However, this is not likely to be the main cause of the validation discrepancy seen in this study, as large porosity was obtained in the Nb_2O_5 electrode and the model could work well for some commercial chemistry between 5 and 10C [46]. The accuracy of the volume-averaging assumption in the DFN model can be further investigated via microscale modelling in the future [47].

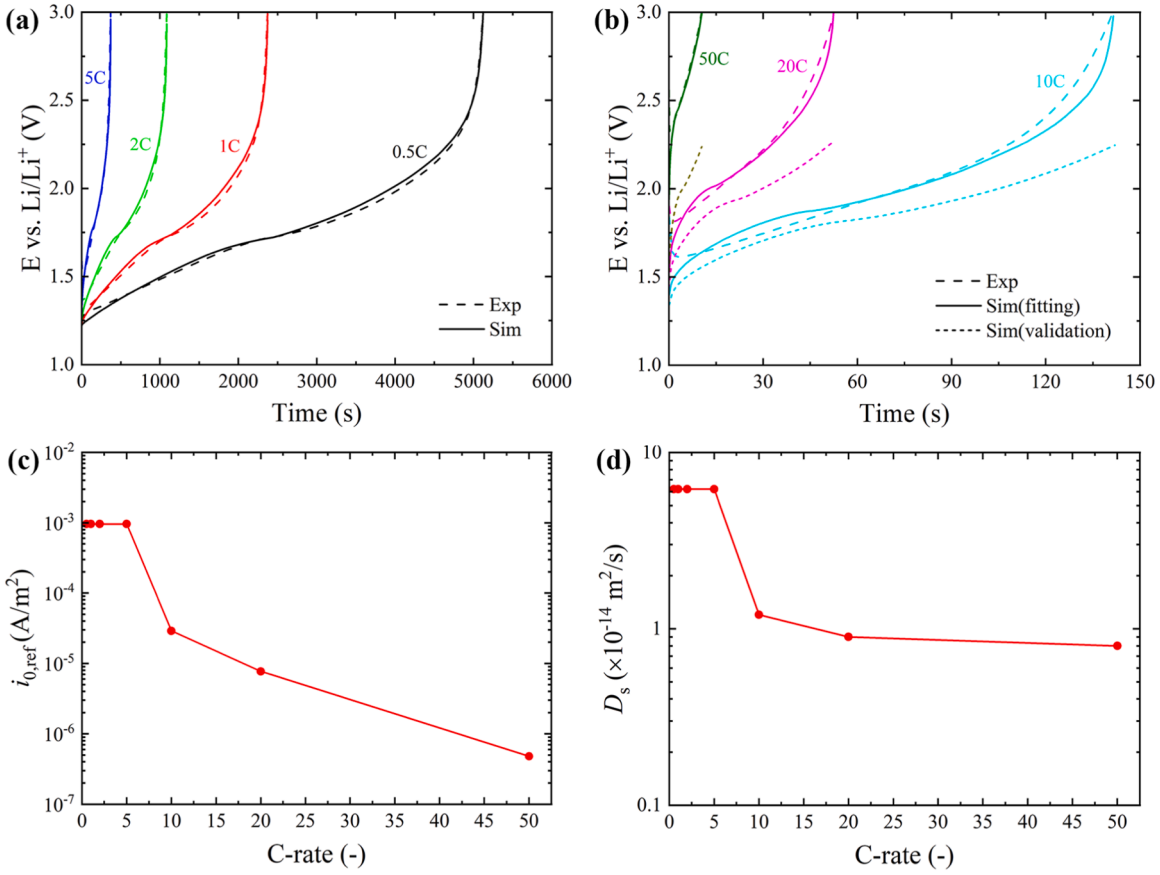

Fig. 6. (a) Experimental (dash line) and simulated (solid line) cell voltage at 0.5−5C charge rates. (b) Experimental (dash line), simulated by fitting (solid line) and simulated by validation (short dash line) cell voltage at 10−50C charge rates. Data at 0.5C was used for model parameterization to obtain (c) reference exchange-current density $i_{0,ref}$ and (d) solid-state diffusivity D_s of Nb_2O_5 and validate at 1−5C. The model parameters obtained at 0.5C was also validated at 10−50C (short dash line) and were refitted at each C-rate to simulate the cell voltage (solid line). The fitted values of $i_{0,ref}$ and D_s are also given in (c) and (d).

In general, we have demonstrated that the physicochemical properties of Nb_2O_5 are stable at C-rates below 5C and the DFN model can accurately simulate the material's electrochemical response. The effective properties at higher C-rates appear to be rate-dependent, which informs the variation of Nb_2O_5's charge storage mechanisms. Through the input of fitted parameters, the DFN model can predict the cell performance over a wide range of C-rates. The model can be significantly useful in cell design, simulation, and diagnostics, when the Nb_2O_5 material is combined with other cathode materials and scaled up to battery devices.

5. Conclusions

A DFN electrochemical model was developed for Nb_2O_5 as a high-rate battery anode material. The electrochemical performance of a commercial Nb_2O_5 material was investigated for model development and physicochemical parameterization. The Nb_2O_5 material was a mixture of T-Nb_2O_5 and H-Nb_2O_5 phases and possessed large-size porous polycrystalline particles in rod and ball structure which were formed by amalgamation of many nano-sized particles.

CV and rate capability tests were performed on the Nb_2O_5 material using coin cells. A quantitative analysis of the material's CV showed that the capacitive contribution to charge storage varied from 15.6 to 53.4% when the scan rate was increased from 0.1 to 5 mV s^{-1}. Hence the charge storage of the present Nb_2O_5 was dominated by diffusion-controlled lithium insertion at low scan rates, and the capacitive effects started to play a vital role at higher scan rates. The average charge capacities for the Nb_2O_5 material were 143 (0.5C), 132 (1C), 120 (2C), 102 (5C), 78 (10C), 58 (20C) and 29 (50C) mAh g^{-1}, respectively. The material showed an excellent capacity retention of more than 55% when the applied current is below 10C.

The DFN model was applied to simulate the rate performance of the present Nb_2O_5. The exchange-current density and solid-state diffusivity of Nb_2O_5 was parameterized at 0.5C to be 9.6×10^{-4} A m^{-2} and 6.2×10^{-14} m^2 s^{-1}, respectively. Further validation of the model parameters at other higher C-rates proved that the DFN model was highly reliable for C-rates up to 5C. Beyond 5C, apparent modifications of the material properties had to be made by refitting the model. This provided us insightful information of the change in the material's electrochemical behavior. The drop of exchange-current density and solid-state diffusivity by 1−3 orders of magnitude at 10−50C revealed that the charge storage mechanism was gradually dominated by capacitive effects which agreed well with the experimental observations but have not been sufficiently considered in the present DFN model.

CRediT authorship contribution statement

Jie Lin: Conceptualization, Methodology, Investigation, Writing – original draft. **Siyu Zhao:** Conceptualization, Methodology, Investigation, Writing – original draft. **Thomas G. Tranter:** Software, Resources, Writing – review & editing. **Zhenyu Zhang:** Formal analysis, Resources. **Fei Peng:** Investigation, Resources. **Dan Brett:** Supervision, Project administration, Funding acquisition. **Rhodri Jervis:** Writing – review & editing, Supervision, Project administration, Funding acquisition. **Paul R. Shearing:** Writing – review & editing, Supervision, Project administration, Funding acquisition.

Declaration of Competing Interest

The authors declare that they have no known competing financial interests or personal relationships that could have appeared to influence the work reported in this paper.

Data availability

Data will be made available on request.

Acknowledgments

This work was supported by the Innovate UK project Cathode and Anode Supply Chain for Advanced Demonstrator (CASCADE), grant number 10007489, and the Faraday Institution Multiscale Modelling and SOLBAT projects (Faraday.ac.uk; EP/S003053/1, grant numbers FIRG003, FIRG025 and FIRG026). The Royal Academy of Engineering is acknowledged for the financial support of Shearing (CiET1718\59) and Brett (RCSRF2021/13/53) under the Chair in Emerging Technologies and Research Chairs scheme.

Supplementary materials

Supplementary material associated with this article can be found, in the online version, at doi:10.1016/j.electacta.2023.141983.

References

[1] G. Zubi, R. Dufo-López, M. Carvalho, G. Pasaoglu, The lithium-ion battery: State of the art and future perspectives, Renew. Sustain. Energy Rev. 89 (2018) 292–308.
[2] X.G. Yang, T. Liu, Y. Gao, S. Ge, Y. Leng, D. Wang, C.Y. Wang, Asymmetric temperature modulation for extreme fast charging of lithium-ion batteries, Joule 3 (2019) 3002–3019.
[3] D.P. Finegan, A. Quinn, D.S. Wragg, A.M. Colclasure, X. Lu, C. Tan, T.M. M. Heenan, R. Jervis, D.J.L. Brett, S. Das, T. Gao, D.A. Cogswell, M.Z. Bazant, M. Di Michiel, S. Checchia, P.R. Shearing, K. Smith, Spatial dynamics of lithiation and lithium plating during high-rate operation of graphite electrodes, Energy Environ. Sci. 13 (2020) 2570–2584.
[4] P.P. Paul, V. Thampy, C. Cao, H.G. Steinrück, T.R. Tanim, A.R. Dunlop, E.J. Dufek, S.E. Trask, A.N. Jansen, M.F. Toney, J.N. Weker, Quantification of heterogeneous, irreversible lithium plating in extreme fast charging of lithium-ion batteries, Energy Environ. Sci. 14 (2021) 4979–4988.
[5] N. Nitta, F. Wu, J.T. Lee, G. Yushin, Li-ion battery materials: present and future, Mater. Today 18 (2015) 252–264.
[6] M. Lübke, A. Sumboja, I.D. Johnson, D.J.L. Brett, P.R. Shearing, Z. Liu, J.A. Darr, High power nano-Nb_2O_5 negative electrodes for lithium-ion batteries, Electrochim. Acta 192 (2016) 363–369.
[7] H. Ding, Z. Song, H. Zhang, H. Zhang, X. Li, Niobium-based oxide anodes toward fast and safe energy storage: a review, Mater. Today Nano 11 (2020).
[8] V. Augustyn, J. Come, M.A. Lowe, J.W. Kim, P.L. Taberna, S.H. Tolbert, H. D. Abruna, P. Simon, B. Dunn, High-rate electrochemical energy storage through Li + intercalation pseudocapacitance, Nat. Mater. 12 (2013) 518–522.
[9] C. Nico, T. Monteiro, M.P.F. Graça, Niobium oxides and niobates physical properties: review and prospects, Prog. Mater Sci. 80 (2016) 1–37.
[10] A.A. Lubimtsev, P.R.C. Kent, B.G. Sumpter, P. Ganesh, Understanding the origin of high-rate intercalation pseudocapacitance in Nb_2O_5 crystals, J. Mater. Chem. A 1 (2013).
[11] H. Schäfer, R. Gruehn, F. Schulte, The modifications of niobium pentoxide, Angew. Chem. Int. Ed Engl. 5 (1966) 40–52.
[12] K.J. Griffith, A.C. Forse, J.M. Griffin, C.P. Grey, High-rate intercalation without nanostructuring in metastable Nb_2O_5 bronze phases, J. Am. Chem. Soc. 138 (2016) 8888–8899.
[13] P. Barnes, Y. Zuo, K. Dixon, D. Hou, S. Lee, Z. Ma, J.G. Connell, H. Zhou, C. Deng, K. Smith, E. Gabriel, Y. Liu, O.O. Maryon, P.H. Davis, H. Zhu, Y. Du, J. Qi, Z. Zhu, C. Chen, Z. Zhu, Y. Zhou, P.J. Simmonds, A.E. Briggs, D. Schwartz, S.P. Ong, H. Xiong, Electrochemically induced amorphous-to-rock-salt phase transformation in niobium oxide electrode for Li-ion batteries, Nat. Mater. 21 (2022) 795–803.
[14] A. Bowman, T. Wallace, J. Yarnell, R. Wenzel, The crystal structure of niobium monoxide, Acta Crystallogr. 21 (1966) 843, 843.
[15] T. Ikeya, M. Senna, Change in the structure of niobium pentoxide due to mechanical and thermal treatments, J. Non Cryst. Solids 105 (1988) 243–250.
[16] Y. Zhou, K. Liu, Y. Zhou, J.-h. Ni, A.-c. Dou, M.-r. Su, Y.J. Liu, Synthesis of a novel hexagonal porous TT-Nb_2O_5 via solid state reaction for high-performance lithium ion battery anodes, J. Cent. South Univ. 27 (2021) 3625–3636.
[17] M. Yang, S. Li, J. Huang, Three-dimensional cross-linked Nb_2O_5 polymorphs derived from cellulose substances: insights into the mechanisms of lithium storage, ACS Appl. Mater. Interfaces 13 (2021) 39501–39512.
[18] H. Park, D. Lee, T. Song, High capacity monoclinic Nb_2O_5 and semiconducting NbO_2 composite as high-power anode material for Li-Ion batteries, J. Power Sources 414 (2019) 377–382.
[19] X. Wang, G. Li, Z. Chen, V. Augustyn, X. Ma, G. Wang, B. Dunn, Y. Lu, High-performance supercapacitors based on nanocomposites of Nb_2O_5 nanocrystals and carbon nanotubes, Adv. Energy Mater. 1 (2011) 1089–1093.
[20] X. Chen, K. Liu, Q. Qin, Z. Yu, M. Li, X. Qu, Y. Zhou, A. Dou, M. Su, Y. Liu, High-rate capability of carbon-coated micron-sized hexagonal TT-Nb_2O_5 composites for lithium-ion battery, Ceram. Int. 47 (2021) 15400–15407.
[21] K.J. Griffith, K.M. Wiaderek, G. Cibin, L.E. Marbella, C.P. Grey, Niobium tungsten oxides for high-rate lithium-ion energy storage, Nature 559 (2018) 556–563.
[22] X. Chen, X. Liu, S. Hao, J. Wang, N. Ahmad, P. Zhang, P. Cui, M. Su, A. Dou, Y. Zhou, Y. Liu, Synthesis and performance of micron-sized hexagonal $W_{0.025}Nb_{1.97}O_5$ for high-rate lithium-ion batteries, Ceram. Int. 48 (2022) 27815–27822.
[23] T. Brezesinski, J. Wang, S.H. Tolbert, B. Dunn, Ordered mesoporous alpha-MoO3 with iso-oriented nanocrystalline walls for thin-film pseudocapacitors, Nat. Mater. 9 (2010) 146–151.
[24] J. Come, V. Augustyn, J.W. Kim, P. Rozier, P.L. Taberna, P. Gogotsi, J.W. Long, B. Dunn, P. Simon, Electrochemical kinetics of nanostructured Nb_2O_5 electrodes, J. Electrochem. Soc. 161 (2014) A718–A725.
[25] Z. Zhou, S. Lou, X. Cheng, B. Cui, W. Si, F. Ding, Y. Ma, P. Zuo, C. Du, J. Wang, Superior electrochemical performance of WNb_2O_8 nanorods triggered by ultra-efficient Li+ diffusion, ChemistrySelect 5 (2020) 1209–1213.
[26] N. Kumagai, Y. Koishikawa, S. Komaba, N. Koshiba, Thermodynamics and kinetics of lithium intercalation into Nb_2O_5 electrodes for a 2 V rechargeable lithium battery, J. Electrochem. Soc. 146 (1999) 3203.
[27] A.N. Mistry, K. Smith, P.P. Mukherjee, Electrochemistry coupled mesoscale complexations in electrodes lead to thermo-electrochemical extremes, ACS Appl. Mater. Interfaces 10 (2018) 28644–28655.
[28] J. Lin, H.N. Chu, C.W. Monroe, D.A. Howey, Anisotropic thermal characterisation of largge-format lithium-ion pouch cells, Batter. Supercaps (2022), e202100401.
[29] G. Li, C.W. Monroe, Multiscale lithium-battery modeling from materials to cells, Annu. Rev. Chem. Biomol. Eng. 11 (2020) 277–310.
[30] G.L. Plett, Battery management systems: battery modeling, artech house 2015.
[31] M. Doyle, T.F. Fuller, J. Newman, Modeling of galvanostatic charge and discharge of the lithium/polymer/insertion cell, J. Electrochem. Soc. 140 (1993) 1526–1533.
[32] M. Doyle, J. Newman, A.S. Gozdz, C.N. Schmutz, J.M. Tarascon, Comparison of modeling predictions with experimental data from plastic lithium ion cells, J. Electrochem. Soc. 143 (1996) 1890.
[33] T.F. Fuller, M. Doyle, J. Newman, Simulation and optimization of the dual lithium ion insertion cell, J. Electrochem. Soc. 141 (1994) 1–10.
[34] X. Lu, A. Bertei, D.P. Finegan, C. Tan, S.R. Daemi, J.S. Weaving, K.B. O'Regan, T.M. M. Heenan, G. Hinds, E. Kendrick, D.J.L. Brett, P.R. Shearing, 3D microstructure design of lithium-ion battery electrodes assisted by X-ray nano-computed tomography and modelling, Nat. Commun. 11 (2020) 2079.
[35] X.G. Yang, T. Liu, C.Y. Wang, Thermally modulated lithium iron phosphate batteries for mass-market electric vehicles, Nat. Energy 6 (2021) 176–185.
[36] S. Xu, K.H. Chen, N.P. Dasgupta, J.B. Siegel, A.G. Stefanopoulou, Evolution of dead lithium growth in lithium metal batteries: experimentally validated model of the apparent capacity loss, J. Electrochem. Soc. 166 (2019) A3456–A3463.
[37] V. Sulzer, S.G. Marquis, R. Timms, M. Robinson, S.J. Chapman, Python battery mathematical modelling (PyBaMM), J. Open Res. Softw. 9 (2021).
[38] T.G. Tranter, R. Timms, T.M.M. Heenan, S.G. Marquis, V. Sulzer, A. Jnawali, M.D. R. Kok, C.P. Please, S.J. Chapman, P.R. Shearing, D.J.L. Brett, Probing heterogeneity in Li-ion batteries with coupled multiscale models of electrochemistry and thermal transport using tomographic domains, J. Electrochem. Soc. 167 (2020).
[39] Q. Hu, Y. Wu, D. Ren, J. Liao, Y. Song, H. Liang, A. Wang, Y. He, L. Wang, Z. Chen, X. He, Revisiting the initial irreversible capacity loss of $LiNi_{0.6}Co_{0.2}Mn_{0.2}O_2$ cathode material batteries, Energy Storage Mater. 50 (2022) 373–379.
[40] Z. Zhang, S. Wu, J. Cheng, W. Zhang, MoS_2 nanobelts with (002) plane edges-enriched flat surfaces for high-rate sodium and lithium storage, Energy Storage Mater. 15 (2018) 65–74.
[41] S. Li, Q. Xu, E. Uchaker, X. Cao, G. Cao, Comparison of amorphous, pseudohexagonal and orthorhombic Nb_2O_5 for high-rate lithium ion insertion, CrystEngComm 18 (2016) 2532–2540.
[42] H. Zhang, Y. Wang, P. Liu, S.L. Chou, J.Z. Wang, H. Liu, G. Wang, H. Zhao, Highly ordered single crystalline nanowire array assembled three-dimensional $Nb_3O_7(OH)$ and Nb_2O_5 superstructures for energy storage and conversion applications, ACS Nano 10 (2016) 507–514.
[43] M. Wei, K. Wei, M. Ichihara, H. Zhou, Nb_2O_5 nanobelts: a lithium intercalation host with large capacity and high rate capability, Electrochem. Commun. 10 (2008) 980–983.
[44] J. Lin, H.N. Chu, D.A. Howey, C.W. Monroe, Multiscale coupling of surface temperature with solid diffusion in large lithium-ion pouch cells, Commun. Eng. 1 (2022).

[45] J. Landesfeind, H.A. Gasteiger, Temperature and concentration dependence of the ionic transport properties of lithium-ion battery electrolytes, J. Electrochem. Soc. 166 (2019) A3079–A3097.
[46] Y. Ye, L.H. Saw, Y. Shi, K. Somasundaram, A.A.O. Tay, Effect of thermal contact resistances on fast charging of large format lithium ion batteries, Electrochim. Acta 134 (2014) 327–337.
[47] X. Lu, X. Zhang, C. Tan, T.M.M. Heenan, M. Lagnoni, K. O'Regan, S. Daemi, A. Bertei, H.G. Jones, G. Hinds, J. Park, E. Kendrick, D.J.L. Brett, P.R. Shearing, Multi-length scale microstructural design of lithium-ion battery electrodes for improved discharge rate performance, Energy Environ. Sci. 14 (2021) 5929–5946.